

Dynamic modeling and experimental investigations of a magnetostrictive nozzle–flapper servovalve pilot stage

Proc IMechE Part I:
J Systems and Control Engineering
2016, Vol. 230(3) 244–254
© IMechE 2016
Reprints and permissions:
sagepub.co.uk/journalsPermissions.nav
DOI: 10.1177/0959651815621668
pii.sagepub.com


Yuchuan Zhu^{1,2}, Xulei Yang¹ and Tiantian Fu¹

Abstract

A magnetostrictive nozzle–flapper servovalve pilot stage is presented in this article, which is directly driven by a giant magnetostrictive actuator and features three nozzles for the development of large flow rate servovalve. According to the energy conversion sequence in this servovalve, a giant magnetostrictive actuator magnetization model, a giant magnetostrictive material rod eddy loss model and a servovalve dynamic pressure model are all established to enable quantitative depiction and modelling of the dynamic pressure response process of magnetostrictive nozzle–flapper servovalve pilot stage. Consequently, the matched simulation model of the magnetostrictive nozzle–flapper servovalve pilot stage with the mathematic model is followed to be established, and two unknown parameters of complex permeability are determined using the test data from the giant magnetostrictive actuator. By running this simulation model, flapper displacement and output pressure under different structural parameters and variational excited frequencies are determined, certain parameters that are sensitive to the dynamic characteristics of magnetostrictive nozzle–flapper servovalve pilot stage driven by giant magnetostrictive actuator are found and the accompanying rules are revealed. Finally, the experimental system of a magnetostrictive nozzle–flapper servovalve pilot stage driven by giant magnetostrictive actuator was built; both the step-input voltage response curve and the sine-input voltage response curve were captured; and these curves show that the amplitude bandwidth (-3 dB) and the phase bandwidth (-90°) of a magnetostrictive nozzle–flapper servovalve pilot stage can approach 150 and 110 Hz, respectively, which exhibit good agreement with the simulation results. Therefore, the magnetostrictive nozzle–flapper servovalve pilot stage offers a very promising prospect of the novel servovalves with the high-frequency response and the large flow rate.

Keywords

System modeling, system simulation, servohydraulic systems, dynamic modeling, physical modelling

Date received: 16 September 2015; accepted: 15 November 2015

Introduction

A traditional double nozzle–flapper servovalve consists of a permanent magnet torque motor or force motor, a double nozzle–flapper pilot valve and a sliding spool main valve.¹ Permanent magnet torque motors or force motors are most widely used to stroke servovalves which convert low-power electrical excitations into rotational or translational motion, and the torque/force produced is proportional to the exciting current. Due to the low power of torque motors or force motors and the small flow rate gain of the double nozzle–flapper valve, their application in large flow rate servovalves is limited.

Continuous development must be performed to achieve excellent design of servovalves. An important issue is improving the actuating dynamics of the

electromechanical transformer and the pilot-operated stage hydraulic-amplifier flow gain. This is an area that can benefit from applying smart materials, such as magnetic fluids, piezoelectric materials, magnetostrictive materials and designing new structure pilot-operated valves, such as deflector jet valves and multi-nozzle flapper valves.

¹College of Mechanical and Electrical Engineering, Nanjing University of Aeronautics and Astronautics, Nanjing, China

²Department of Aerospace Engineering, University of Maryland, College Park, MD, USA

Corresponding author:

Yuchuan Zhu, College of Mechanical and Electrical Engineering, Nanjing University of Aeronautics and Astronautics, Nanjing 210016, China.
Email: meeyczhu@nuaa.edu.cn

To improve the dynamic performance of servovalves, many studies have focused on the new torque motors or electromagnetic actuators. Li et al.² investigated the influence of magnetic fluids on the dynamic characteristics of permanent magnet torque motors; the results show that magnetic fluid can increase the efficiency of the magnetic circuit and improve the characteristics of torque motors. An energy-saving electro-pneumatic servovalve³ and a direct-drive servo valve⁴ driven by a voice coil motor (VCM) are also presented. Lindler and Anderson⁵ and Zhou and Tian⁶ present a single-stage servovalve using a direct-drive piezoelectric actuator, which offers the potential for faster response compared with traditional two-stage servovalves. Bang et al.⁷ investigated two-stage high-speed electro-hydraulic servovalve using stack-type piezoelectric-elements, and Sangiah et al.⁸ developed a piezoelectric first-stage actuator to move a servovalve spool using the deflector jet principle which is especially suited for aerospace actuation requirements. Hiratsuka and Urai⁹ designed a giant magnetostrictive actuator (GMA)-based direct-drive servovalve with a 650-Hz bandwidth (-3 dB) but a flow rate of only 2 L/min. In 2001, Urai and Tanaka¹⁰ again presented a servovalve using a giant magnetostrictive tandem actuator with a 250-Hz bandwidth (-3 dB) and a 50 L/min flow rate. In 2002, a GMA based pneumatic and hydraulic single nozzle-flapper-type servovalve^{11–13} was analysed and tested. The results showed that the new servovalve's step rise time is less than 1 ms and that it has a 680-Hz bandwidth (-3 dB). In 2010, Karunanidhi and Singaperumal¹⁴ designed, built and integrated a GMA into an existing flapper-nozzle servovalve; the experimental results demonstrated that the valve step response driven by a GMA can reach 7.8 ms, which is faster than the 11.2-ms response achieved by the conventional torque motor. In 2011, a jet-pipe servovalve^{15,16} driven by a GMA was presented and discussed, in which the use of 0.5 A input current amplitude, the -3 dB bandwidth was approximately 350 Hz the -3 dB valve bandwidth was approximately 350 Hz under the 0.5 A input current amplitude excitation. In 2015, a four-nozzle flapper servovalve driven by a GMA is developed.¹⁷

Moreover, in order to improve the performance of the pilot-operated valve in two-stage servovalve, Aung and Li¹⁸ carried out a numerical study of cavitation phenomenon in a flapper-nozzle pilot stage with different flapper shapes. A computational fluid dynamics (CFD) analysis of flow forces and energy loss characteristics in a flapper-nozzle pilot valve with different null clearances is presented.¹⁹ The characteristic research²⁰ of the flow field in the flapper-nozzle pilot stage is performed; the results show that the increment of inlet pressure intensifies cavitation in the flapper-nozzle pilot stage and induces the shedding phenomenon. The discharge characteristics of spool valve orifices are simulated by the CFD method and a formula for discharge coefficient and Reynolds number is derived.²¹

In conclusion, the existing studies suggest that the dynamic characteristics of a traditional servovalve can be improved by redesigning the structure of the servovalve and incorporating smart materials, such as piezoelectric materials and magnetostrictive materials. Among these smart materials, giant magnetostrictive materials (GMMs) have the following characteristics: large strain, high reliability, large energy density, fast response, broad bandwidth and intelligent response.^{22–24} GMMs enabled the development of a totally new class of electromechanical devices with higher energy density, faster response and better precision than previously possible.^{25–29} GMAs are one of the most exciting new actuator technologies available today and have revealed new design options for mechanical and electrical engineers alike.

Generally, it is difficult to achieve high-frequency response for a large flow servovalve; however, a multi-nozzle valve configuration such as three-nozzle can increase the flow gain observably without substantially slowing response; in addition, the use of fast and stiff magnetostrictive actuators as valve drives offers advantages for valve characteristics concerning high frequency and large output power; thus, this article reports the dynamic response investigations of a novel servovalve concept distinguished by three-nozzle structures and GMA direct driving, which have the potential to provide faster response and higher flow rate than traditional double nozzle-flapper servovalves driven by permanent magnet torque motors did and offer very promising prospects of the novel servovalves with the high-frequency response and the large flow rate.

Valve configuration and energy transformation process

Figure 1 shows the configuration of magnetostrictive nozzle-flapper servovalve pilot stage (MNSP), which consists of a GMA (left) and a three-nozzle flapper valve (right). A GMA mainly includes adjusting bolt, coils, shell, GMM rod and output rod (flapper), and a three-nozzle flapper valve mainly consists of the flapper, the fixed orifice and the three nozzles. The operating principle of MNSP is as follows: the oil is supplied to the servovalve from the fixed orifices to the nozzles and the oil pressure control port; when the coils are excited and generate the applied field, the GMM rod elongates; meanwhile, the clearance between the flapper and the nozzle is changed, and thus, the control pressure varied in proportion with the excited current accordingly. In addition, a cooling and thermal compensation system is designed to address the issue that the thermal expansion of the GMM rod weakens the precision of servovalve; the leakage oil flows in the direction as shown in Figure 1, which can cool the coil and keep the temperature of the coil close to the temperature of shell; under this situation, the temperature rise of the coil leads to GMM rod thermal expansion

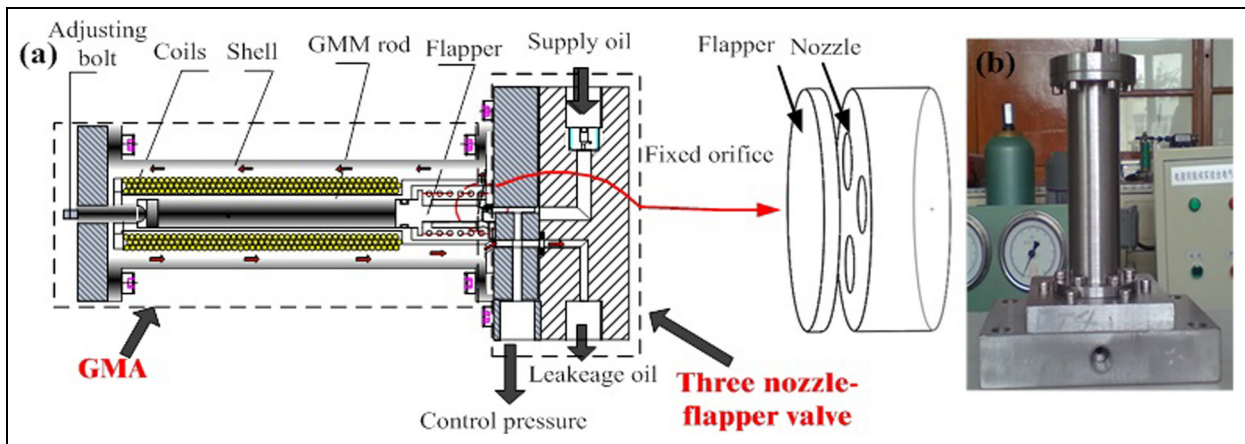


Figure 1. MNSP valve: (a) valve configuration and (b) valve photograph.

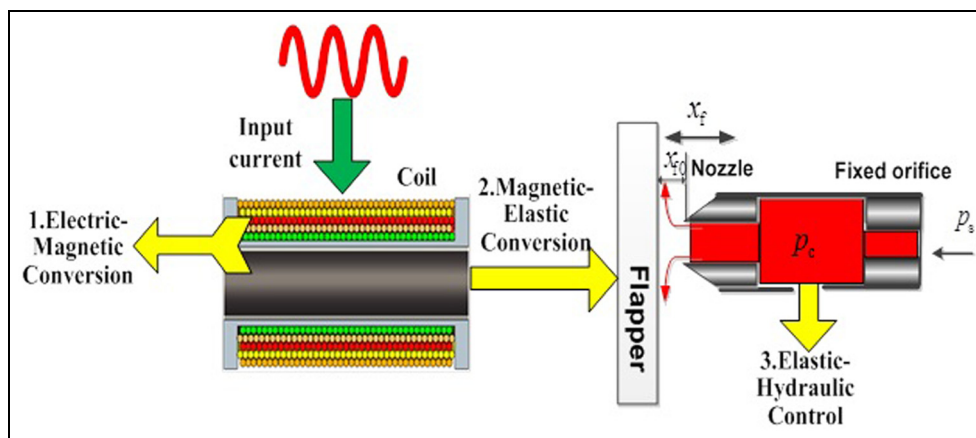


Figure 2. Schematic diagram of MNSP energy conversion and control process.

and the temperature rise of the shell leads to the thermal expansion itself which can be transferred to the adjusting bolt; thus, the adjusting bolt moves left to compensate the thermal expansion of the GMM rod, thus, the thermal compensation precision can be ensured by designing the length and the thermal expansion coefficient of shell.

As shown in Figure 2, the energy conversion and control process in an MNSP involves three stages: the first stage from the electrical energy to the magnetic energy, the second stage from magnetic energy to the elastic potential energy and the third stage to control the hydraulic energy by the elastic potential energy.

In the first stage, electrical–magnetic energy transformation is achieved, which can be depicted by the magnetization model to describe the relationship between the exciting current and the magnetization of the GMM rod. Meanwhile, in this stage, it should not be neglected that the eddy current in the GMM rod weakens the electrical–magnetic energy transformation efficiency and can be modelled by the dynamic magnetization model with eddy loss.

In the middle-stage implements, a magnetoelastic energy transformation can be modelled by the magnetoelastic model to describe the relationship between the

magnetostrictive strain and the magnetization intensity of the GMM rod; in this stage, the GMM rod can be abstracted into unidimensional elastic body and then the magnetization intensity of the GMM rod would lead to a magnetostrictive force which can be depicted by quadratic domain rotation model and Hooke's law; thus, the dynamic behaviour of GMM rod in this stage can be described by spring–dashpot–mass model, that is, a strain-based dynamic displacement of the GMM rod would be governed by the magnetization intensity; in addition, the flow force result from the nozzle–flapper valve would act on the GMM rod as a load.

In the final stage, the hydraulic energy controlled by the elastic potential energy is obtained, and the strain-based dynamic displacement of the GMM rod would be transmitted to the flapper, which would regulate the clearance between the flapper and nozzle to change the control pressure in the chamber between the fixed orifice and nozzle.

Dynamic performance model

Based on the energy conversion process in an MNSP, the dynamic model of an MNSP involves five

submodels from the viewpoint of energy conversion and control: the magnetization model of the GMM rod without eddy current effect, the magnetization model of the GMM rod with eddy current effect, the magnetoelastic model of the GMM rod, the flow force model on the flapper and the dynamic control pressure model in the chamber between the fixed orifice and nozzle.

Magnetization model of GMM rod without eddy current effect

The applied magnetic field H generated by an alternating current i is given by

$$H = \frac{Ni}{k_f L_G} = \frac{NI_m}{k_f L_G} \cos \omega t = H_m \cos \omega t \quad (1)$$

where N is the number of the excitation coil turns, I_m is the amplitude of the alternating current, k_f is the leakage coefficient of the magnetic flux, L_G is the length of the GMM rod, H_m is the amplitude of the applied magnetic field and ω is the angular frequency.

In a sinusoidal magnetic field, the relative permeability of a GMM rod is a complex number, and the magnetization M can be deduced from the applied magnetic field H [17]

$$M = \sqrt{\left(\sqrt{|\mu_r|^2 - (\mu_h'')^2} - 1\right)^2 + (\mu_h'')^2} H_m \cos(\omega t - \theta_h) \quad (2)$$

where μ_h'' is the imaginary part of the complex relative permeability and μ_r is the relative permeability.

The lag angle θ_h caused by hysteresis is

$$\theta_h = \arctan\left(\frac{\mu_h''}{\sqrt{|\mu_r|^2 - (\mu_h'')^2} - 1}\right) \quad (3)$$

Magnetization model of GMM rod with eddy current effect

When the GMM rod is excited by high-frequency alternating current, the eddy loss occurs in the GMA, which will decrease its response speed. The magnetization intensity M in the GMM rod can be written as

$$M = (|\mu_r| - 1)H \quad (4)$$

The energy of magnetization for the eddy loss in the dynamic state can be written as³⁰

$$\begin{aligned} \mu_0 \int M_{\text{eddy}} dH_c &\approx \mu_0^2 \int \frac{D_G^2}{2\rho\beta} \left(\frac{dM}{dt}\right)^2 dt \\ &= \mu_0^2 \frac{D_G^2}{2\rho\beta} \int \frac{dM}{dt} \frac{dM}{dH_c} \frac{dH}{dt} dt \end{aligned} \quad (5)$$

where μ_0 is the permeability of the free space, M_{eddy} is the magnetization intensity for the eddy loss; ρ and D_G

are the electrical resistivity and the diameter of the GMM rod, respectively; and β is a geometrical factor.

Taking the derivative with respect to t of both the sides of equation (5) leads to

$$M_{\text{eddy}} \approx \mu_0 \frac{D_G^2}{2\rho\beta} \frac{dM}{dt} \frac{dM}{dH} = \mu_0 (|\mu_r| - 1) \frac{D_G^2}{2\rho\beta} \frac{dM}{dt} \quad (6)$$

Consequently, the energy equation for the eddy loss based on equation (6) is

$$\int M dH = \int (|\mu_r| - 1) H dH - \int M_{\text{eddy}} dH \quad (7)$$

Taking the derivative with respect to H_c of both the sides of equation (7) leads to

$$\begin{aligned} M &= \mu_0 |\mu_r| H - M_{\text{eddy}} = (|\mu_r| - 1)H \\ &\quad - \mu_0 (|\mu_r| - 1) \frac{D_G^2}{2\rho\beta} \frac{dM}{dt} \end{aligned} \quad (8)$$

Taking the Laplace transform of equation (8), the actual magnetization intensity M in the GMM rod becomes

$$M = \frac{(|\mu_r| - 1)H}{\mu_0 (|\mu_r| - 1) \frac{D_G^2}{2\rho\beta} s + 1} = \frac{(|\mu_r| - 1)H}{\tau s + 1} \quad (9)$$

where $\tau = \mu_0 (|\mu_r| - 1) (D_G^2 / 2\rho\beta)$ is the eddy time constant.

Magnetoelastic model of GMM rod

Under the excitation from driving magnetic field, the magnetostrictive rate $\lambda = \Delta\lambda/\lambda$ describes the relative change quantity in length of the GMM rod; based on the quadratic domain rotation model,³¹ the magnetostrictive rate λ is given by

$$\lambda = \frac{3}{2} \frac{\lambda_S}{M_S^2} M^2 \quad (10)$$

where λ_S and M_S are the saturation magnetostriction and the saturation magnetization, respectively.

The process of magnetic–mechanic coupling can be expressed by Figure 3. When the magnetic field intensity is changed within a limited range, following Hooke's law, the magnetostrictive force generated by the GMM rod can be approximately defined as

$$F = A_G E_G \lambda \quad (11)$$

where A_G is the cross-sectional area of the GMM rod, E_G is the elasticity modulus of the GMM rod and λ is the magnetostrictive rate.

The force balance equation of GMA is

$$F = m_e \frac{d^2 x_f}{dt^2} + B_e \frac{dx_f}{dt} + k_e x_f + F_L \quad (12)$$

where x_f is the strain-based displacement of GMM rod, which is the same with the displacement of flapper; m_e

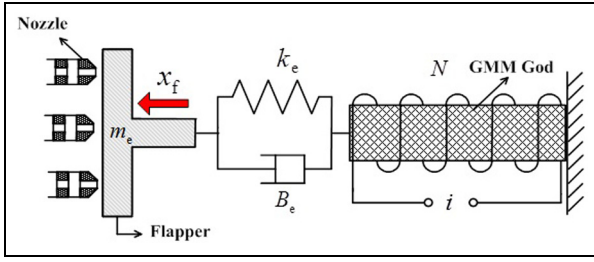


Figure 3. Sketch of GMA magnetic–mechanic coupling.

is the equivalent mass of GMM rod; $m_e = m_1/2 + m_2$, m_1 and m_2 are the mass of the GMM and output rods, respectively; B_e is the equivalent damping coefficient; k_e is the equivalent stiffness coefficient for the GMM rod, $k_e = A_G E_G / L_G$; and F_L is the flow force of oil from the nozzle to the flapper.

Based on equations (10)–(12), the magnetoelastic model of the GMM rod which described the process from the magnetic intensity to the strain-based displacement of GMM rod can be written as

$$\frac{3 \lambda_S}{2 M_S^2} M^2 A_G E_G = m_e \frac{d^2 x_f}{dt^2} + B_e \frac{dx_f}{dt} + k_e x_f + F_L \quad (13)$$

Flow force model on the flapper

Flow force is the force applied on the flapper, which can be shown by Figure 4 according to the nozzle–flapper configuration in Figure 1; using Bernoulli's equation, the flow force can be written as follows

$$F_L = 3 p_N A_N + 3 \rho q_1 v_1 \quad (14)$$

where A_N is the area of the plane of the nozzle diameter, v_1 is the fluid velocity at the plane of the nozzle diameter, q_1 is the flow rate through the nozzle and p_N is the static pressure of the plane of the nozzle diameter, which can be written as follows based on Bernoulli's equation

$$p_N = p_c - \frac{1}{2} \rho v_1^2 \quad (15)$$

where p_c is the pressure of control chamber between the fixed orifice and nozzle.

Combining equations (14) and (15), we obtain

$$F_L = 3 \left(p_c + \frac{1}{2} \rho v_1^2 \right) A_N \quad (16)$$

Meanwhile, v_1 can be written as follows

$$v_1 = \frac{q_1}{A_N} = \frac{4 C_{df} (x_{f0} - x_f) \sqrt{2 p_c / \rho}}{D_N} \quad (17)$$

where x_{f0} , x_f , D_N and C_{df} are the flapper position at null, flapper displacement, nozzle diameter and nozzle discharge coefficient, respectively.

Substituting equation (17) into equation (16) yields

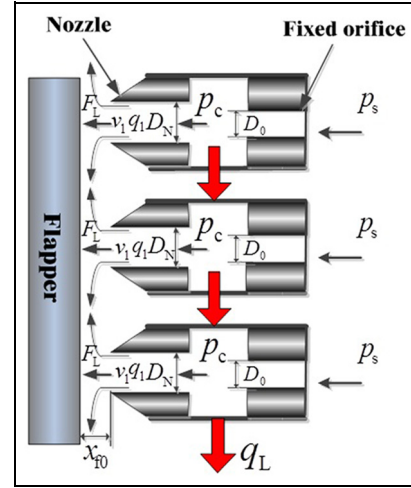


Figure 4. A flow force diagram at the nozzle–flapper.

$$F_L = 3 p_c A_N \left[1 + \frac{16 C_{df}^2 (x_{f0} - x_f)^2}{D_N^2} \right] \quad (18)$$

Dynamic control pressure model in the chamber between the fixed orifice and nozzle

As is shown in Figure 4, the load flow of MNSP q_L equation is

$$q_L = C_{d0} A_0 \sqrt{\frac{2}{\rho} (p_s - p_c)} - 3 C_{df} \pi D_N (x_{f0} - x_f) \sqrt{\frac{2}{\rho} p_c} \quad (19)$$

$$\dot{p}_c = \frac{\beta_e}{V_c} q_L \quad (20)$$

where C_{d0} is the flow coefficient of the fixed orifice, A_0 is the area of the fixed orifice, β_e is the effective bulk modulus of hydraulic oil between the fixed orifice and nozzle and V_c is the volume of hydraulic oil between the fixed orifice and nozzle.

If the load is blocked, $q_L = 0$, set $a = (C_{df} \pi D_N x_{f0}) / (C_{d0} A_0)$ and $x_f = 0$ at null, then $p_{c0} = (p_s) / (9a^2 + 1)$. Equation (19) is a nonlinear function, expand equation (19) at null in Taylor series and use the above null boundary conditions and the linear form of equation (19) can be written as

$$\begin{aligned} q_L &= \frac{\partial q_L}{\partial x_f} x_f - \frac{\partial q_L}{\partial p_c} p_c \\ &= C_{d0} A_0 \sqrt{\frac{2}{\rho} p_s} \left(\frac{3a}{x_{f0}} \sqrt{\frac{1}{9a^2 + 1}} x_f - \frac{\sqrt{(9a^2 + 1)^3}}{6ap_s} p_c \right) \end{aligned} \quad (21)$$

Substituting equation (21) into equation (20)

$$\begin{aligned} \dot{p}_c = & \frac{\beta_e}{V_c} C_{d0} A_0 \sqrt{\frac{2}{\rho} p_s} \frac{3a}{x_{f0}} \sqrt{\frac{1}{9a^2 + 1}} x_f \\ & - \frac{\beta_e}{V_c} C_{d0} A_0 \sqrt{\frac{2}{\rho} p_s} \frac{\sqrt{(9a^2 + 1)^3}}{6ap_s} p_c \end{aligned} \quad (22)$$

Laplace transform to equation (22) yields

$$\frac{p_c(s)}{x_f(s)} = \frac{\frac{\beta_e}{V_c} C_{d0} A_0 \sqrt{\frac{2}{\rho} p_s} \frac{3a}{x_{f0}} \sqrt{\frac{1}{9a^2 + 1}}}{s + \frac{\beta_e}{V_c} C_{d0} A_0 \sqrt{\frac{2}{\rho} p_s} \frac{\sqrt{(9a^2 + 1)^3}}{6ap_s}} \quad (23)$$

Therefore, equation (23) is the dynamic control pressure model in the chamber between the fixed orifice and nozzle which described the elastic-hydraulic adjusting process in MNSP.

In addition, the leakage flow rate can be written as follows

$$Q_c = 3C_{df}\pi D_N x_{f0} \sqrt{\frac{p_s}{\rho}} \quad (24)$$

The leakage flow rate is used to cool the coils and compensate the thermal expansion of GMM rod, which can help to reduce the temperature of the GMM rod and improve the precision of servovalve.

Model simulation

Parameter identification

The first unknown parameter is the relative permeability of the GMM rod from magnetization model of the GMM rod; the identification method is as follows.

Coil inductance L with a GMM rod and coil inductance L_0 without a GMM rod in giant magnetostrictive transducer can be related as follows

$$L = |\mu_r| L_0 \quad (25)$$

Thus, we can show that $|\mu_r| = 5$ by measuring the values of L and L_0 around the bias magnetic field.

The other parameter that needs to be identified is the imaginary part of the relative complex permeability μ_h'' . Based on the identification method presented in the literature,³¹ we can determine the imaginary part of the relative complex permeability to be $\mu_h'' = 2.2$. The other parameters are known and shown in Table 1. Accordingly, in addition to the two parameters verified above, the other model parameters are shown in Table 1.

Simulation results and analysis

Step response results. By running the simulation, some parameters that are sensitive to the dynamic characteristics of MNSP are found, and the accompanying rules are obtained. The diameter, length of the GMM rod and equivalent stiffness play more important roles regarding the step response of MNSP than the other parameters.

As Figure 5(a) shows, when the diameter of the GMM rod D_G is 8 mm, the step response time of the steady-state output flapper displacement is approximately 4 ms; however, this value changed to 3 and 2 ms when the value of D_G is 10 and 12 mm, respectively. As Figure 5(b) indicates, for the same step-input signal, accordingly, the steady-state output flapper

Table 1. Related parameters of MNSP.

No.	Name	Symbol	Unit	Value	No.	Name	Symbol	Unit	Value
1	Coil resistance	R	Ω	3	13	Coil turns	N	l	600
2	Coil inductance	L	mH	3	14	Geometrical factor of GMM rod	β	l	16
3	Open-loop gain of amplifier	K_u	l	10^4	15	Length of GMM rod	L_G	mm	80
4	Vacuum permeability	μ_0	H/m	$4\pi \times 10^{-7}$	16	Pressure of oil source	p_s	MPa	7
5	Relative permeability of GMM rod	μ_r	l	5	17	Flapper position at null clearance	x_{f0}	mm	0.06
6	Equivalent mass of GMM rod	m_e	kg	0.2	18	Eddy time constant	τ	l	2.6×10^{-5}
7	Equivalent stiffness	k_e	N/m	2.36×10^6	19	Equivalent damping coefficient of GMM rod	B_e	Ns/m	2000
8	Diameter of nozzle	D_N	mm	1.2	20	Flow coefficient	C_{df}	l	0.8
9	Diameter of fixed orifice	D_0	mm	0.8	21	Diameter of GMM rod	D_G	mm	10
10	Density of GMM rod	ρ_G	kg/m ³	9250	22	Saturation magnetization	M_s	A/m	7.65×10^5
11	Electrical resistivity of GMM rod	ρ	Ω m	6×10^{-7}	23	Bias magnetization	M_b	A/m	2.0×10^5
12	Bulk modulus of elasticity of GMM rod	E_G	GPa	10	24	Saturation magnetostriction	λ_s	l	1005×10^{-6}

GMM: giant magnetostrictive material.

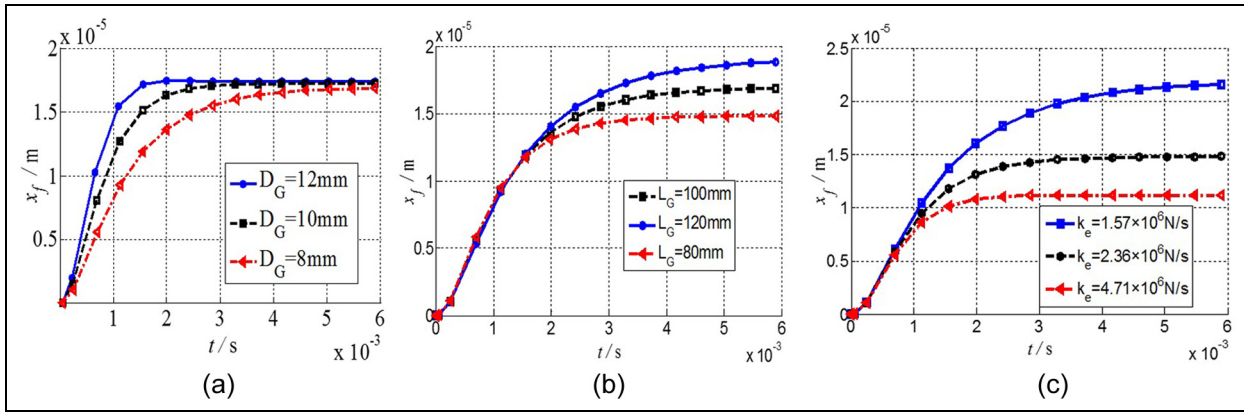


Figure 5. Flapper displacement response curve to a step-input voltage in an MNSP: (a) diameter of the GMM rod, (b) length of the GMM rod and (c) equivalent stiffness.

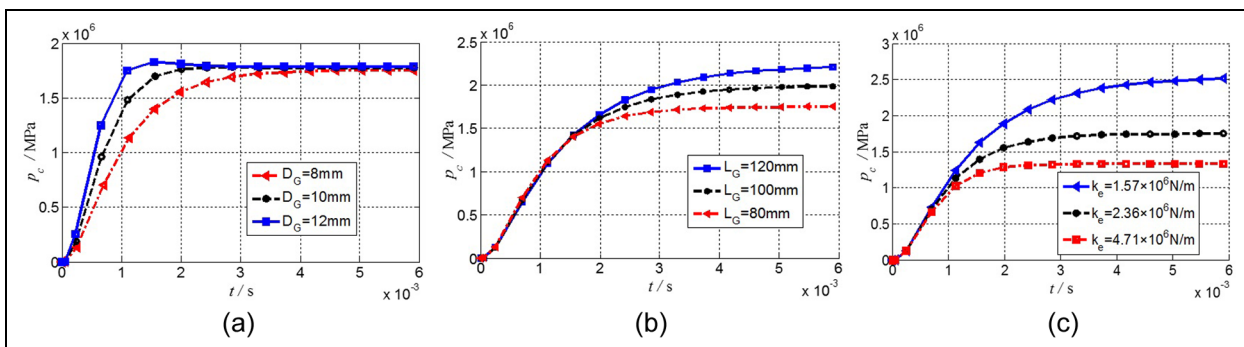


Figure 6. Control pressure response curve to a step-input current in an MNSP: (a) diameter of the GMM rod, (b) length of the GMM rod and (c) equivalent stiffness.

displacement value will reach 15, 17 and 19 μm when the length L_G of the GMM rod is 80, 100 and 120 mm, respectively, and the resulting rise times will be 3, 4 and 5 ms, respectively.

In a similar way, as Figure 5(c) indicates, the steady-state output flapper displacement value will be 10, 15 and 22 μm for equivalent stiffness values k_e of 4.71×10^6 , 2.36×10^6 and $1.57 \times 10^6 \text{N/s}$, respectively, and the resulting rise times will be 2, 4 and 6 ms, respectively.

Similar rules can be found in the control pressure p_c step response curve shown in Figure 6, which confirm that the step response of an MNSP is only controlled by the dynamic response of the GMA and does not depend on the parameters of the flapper valve.

Comparison of sine-response results with hysteresis and eddy current effect. In an MNSP, the dynamic process responding to a sine-input signal involves three sequential stages: (1) from the input voltage to the magnetization of the GMM rod, (2) from the magnetization to the elastic strain of the GMM rod and (3) from the elastic strain of the GMM rod to the fluid control pressure of the MNSP. In the first stage, electromagnetic energy transformation is achieved, the second stage

performed magnetoelastic energy transformation and the final stage results in elastic–hydraulic energy adjusting.

To further distinguish the effect on the dynamic response of an MNSP exerted by electromagnetic, magnetoelastic and elastic–hydraulic energy adjusting process, a group of sine-response curves were constructed, as shown in Figure 7, at excited frequencies from 10 to 250 Hz.

As Figure 7 shows, ‘1’ represents a control pressure curve without static hysteresis, ‘2’ is a control pressure curve with static hysteresis, ‘3’ consists of a magnetization intensity curve without static hysteresis and ‘4’ is a magnetization intensity curve with static hysteresis. Additionally, the left vertical coordinates indicate the magnetization intensity, and the right vertical coordinates indicate the control pressure. The phase lag angles are 36.6° , 17.2° and 5.9° with the driving frequencies 100, 50 and 10 Hz, respectively; moreover, the phase lag angles are 53.4° , 75.4° and 84.7° with the driving frequencies 150, 200 and 250 Hz. In addition, it can be observed that static hysteresis exerts a minor role above 50 Hz. It should be noted that the phase lag angle here is the angle between the magnetization of the GMM rod and the output control pressure, not the

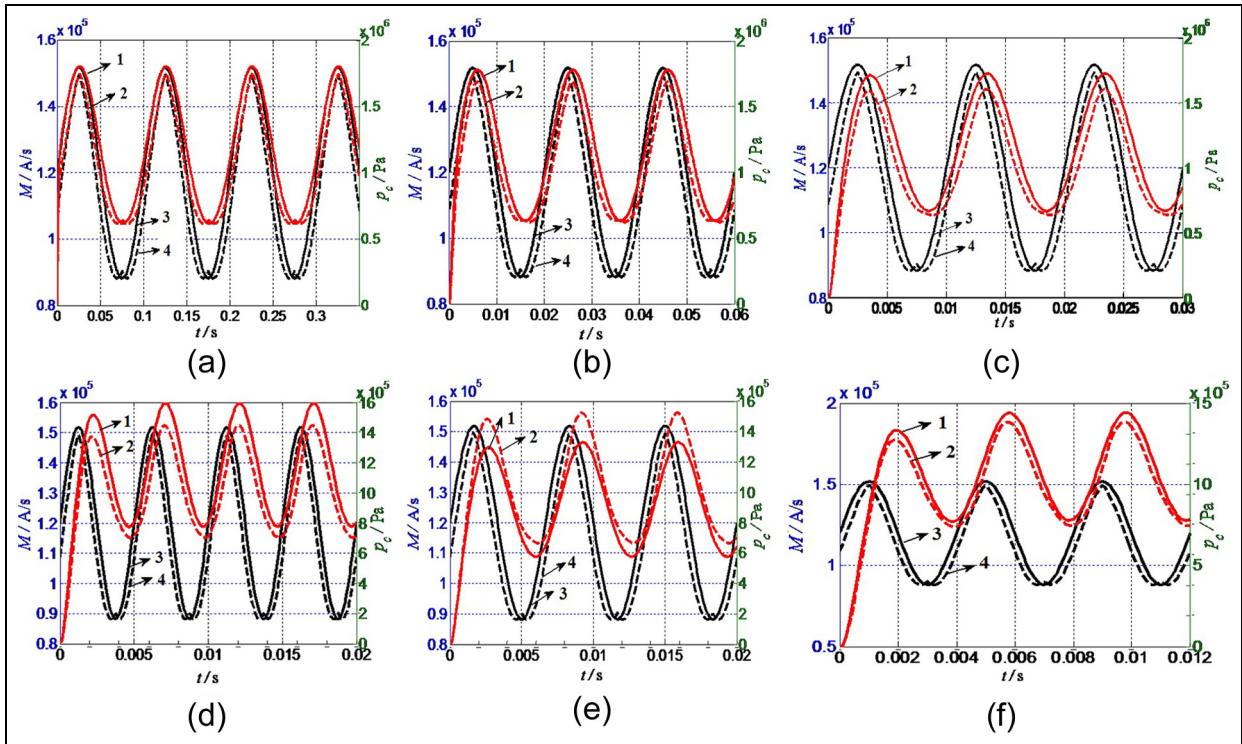


Figure 7. Response curve of magnetization intensity and control pressure to sinusoidal input voltage in an MNSP: (a) 10 Hz, (b) 50 Hz, (c) 100 Hz, (d) 150 Hz, (e) 200 Hz and (f) 250 Hz.

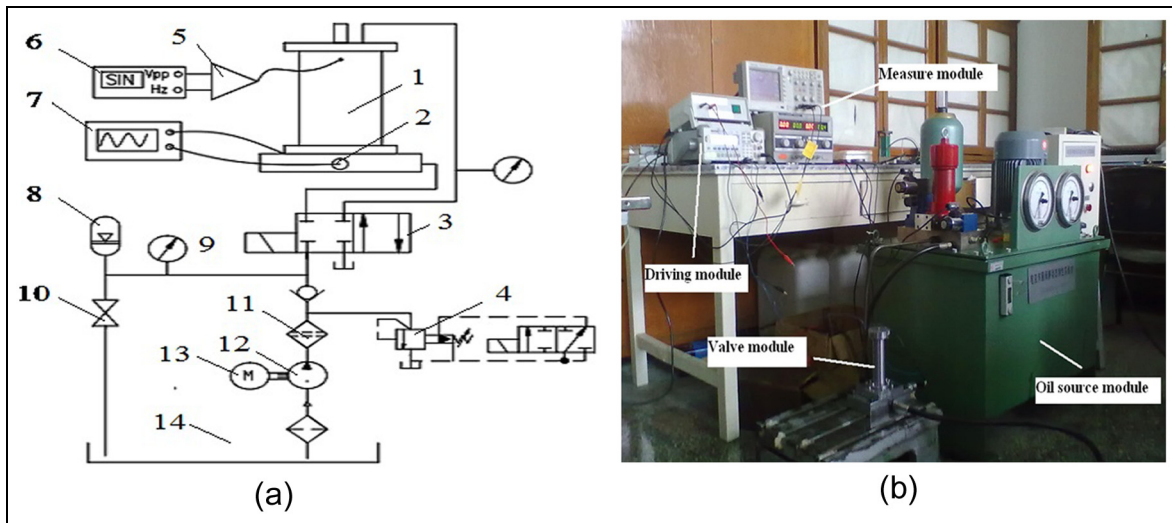


Figure 8. Dynamic testing system for an MNSP: (a) schematic diagram and (b) the experimental set-up. 1: MNSP; 2: pressure sensor; 3: directional valve; 4: electromagnetic relief valve; 5: power amplifier; 6: signal generator; 7: oscilloscope; 8: energy accumulator; 9: precise pressure gage; 10: stop valve; 11: filter; 12: pump; 13: motor; and 14: tank.

angle between the input voltage and the output control pressure, which are much larger than 53.4° , 75.4° and 84.7° with the driving frequencies 150, 200 and 250 Hz because of the eddy current effect of the GMM rod.

Test rigs and test results

Test equipment and test methods

As shown in Figure 8, a model machine (Figure 1(b)) is designed, fabricated, assembled and measured. The

dynamic pressure response data of the model machine valve under a step-input signal and a sinusoidal input signal are collected by a pressure sensor. The test system used to determine the dynamical characteristics of an MNSP consists of an oil source module (rated flow 11.28 L/min and rated pressure 10 MPa), a model valve module, a measure module (pressure sensor M5100, measuring range 0–10 MPa, accuracy $\pm 0.25\%$, oscilloscope TDS1012BSC and driving module (signal generator DG1022)). A schematic and picture of the model

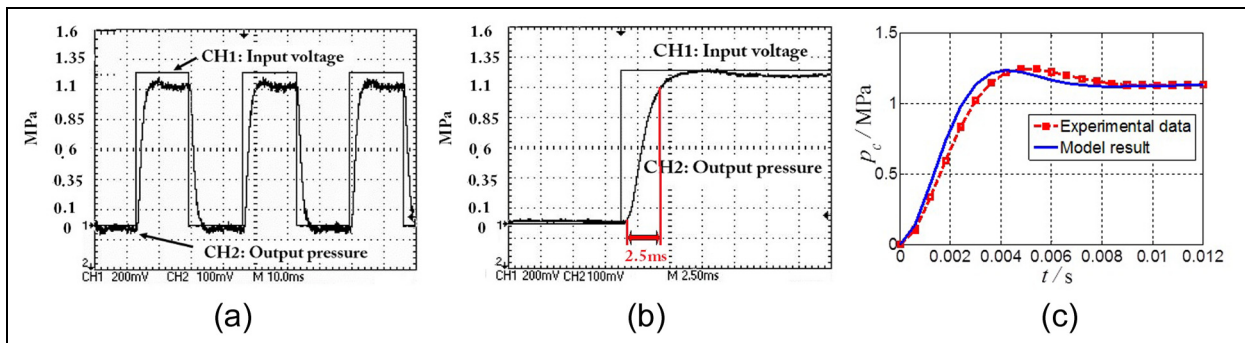


Figure 9. Output pressure response to a step-input current from 0 to 2 A in an MNSP: (a) test data from a square excited voltage, (b) test data from a step excited voltage and (c) test data and model results.

valve test rig are shown in Figure 8(a) and (b), respectively.

The input current electrifying the GMA is generated by a signal generator and a power amplifier and is used to produce the GMA displacement. The control pressure is then generated, measured and transmitted to an oscilloscope.

Step excitation results

The model valve is first excited by a square wave input voltage with an amplitude ranging from 0 to 1 V, the corresponding current from 0 to 2 A and the supply source pressure 7 MPa, and then, the pressure response data from a pressure sensor are recorded by an oscilloscope.

The raw recorded voltage data from pressure sensor are shown in Figure 9(a) and (b); CH1 and CH2 denote the input voltage from signal generator and the output voltage from pressure sensor, respectively. One notable feature in Figure 9(a) and (b) is that the vertical axis scale is 100 mV per grid length for the output pressure and 200 mV for the input voltage; in addition, the horizontal axis scale is 10 ms per grid length for Figure 9(a) and 2.5 ms for Figure 9(b), which can be seen in the bottom of every figure; as shown in Figure 9(b), the 10%–90% rise time of the output pressure is approximately 2.5 ms.

Based on the experimental data in Figure 9(a) and (b), the comparison between the test data and the model results can be seen in Figure 9(c); we can see that this servovalve can achieve a short transition process without ripples and over-adjustment, which shows good agreement with the predicted results of the above-mentioned mathematical model and simulation results.

Sinusoidal excitation results

The pressure response observed with a sinusoidal supply signal is analysed. The operating conditions are supply source pressure 7 MPa and exciting coil current 1 A. The pressure response curves when the voltage

frequency was varied from 30 to 200 Hz were captured by an oscilloscope and are presented in Figure 10.

The raw recorded voltage data from pressure sensor are shown in Figure 10(a)–(f); CH1 and CH2 denote the input voltage from signal generator and the output voltage from pressure sensor, respectively. One notable feature in Figure 10 is that the vertical axis scale is 500 mV per grid length for the output pressure in Figure 10(a)–(d), 200 mV in Figure 10(e) and (f) and 100 mV for the input voltage in Figure 10(a)–(f); in addition, the horizontal axis scale is 25 ms per grid length for Figure 10(a), 10 ms for Figure 10(b)–(d) and 5 ms for Figure 10(e) and (f), which can be seen in the bottom of every figure.

As shown in Figures 10 and 11, for the input voltage, when its amplitude is constant and its frequency varies from 30 to 200 Hz in the sinusoidal wave, the measured amplitude of the output control pressure from the pressure sensor according to around 150 Hz reduces to 70.7% that of around 30 Hz. Meanwhile, when the phase lag angle between the input voltage and output control pressure is around 90° and the input voltage frequency reaches to around 110 Hz, which are in good agreement with the prediction results from the presented model, as shown in Figure 11.

Conclusion

In this article, a servovalve configuration, known as MNSP, is presented. The primary focus of the research was the dynamic pressure characteristics of the MNSP. A GMA magnetization model, which included the complex magnetic permittivity and can describe the static hysteresis of GMA, is first built. Then, a GMA magnetization model with eddy loss is obtained based on the magnetic–elastic energy transformation principle. Finally, the dynamic control pressure model is deduced based on the elastic–hydraulic conversion.

By running this simulation model, the relationship between the flapper displacement and control pressure is determined under different structural parameters and the excited frequency; accordingly, some structural

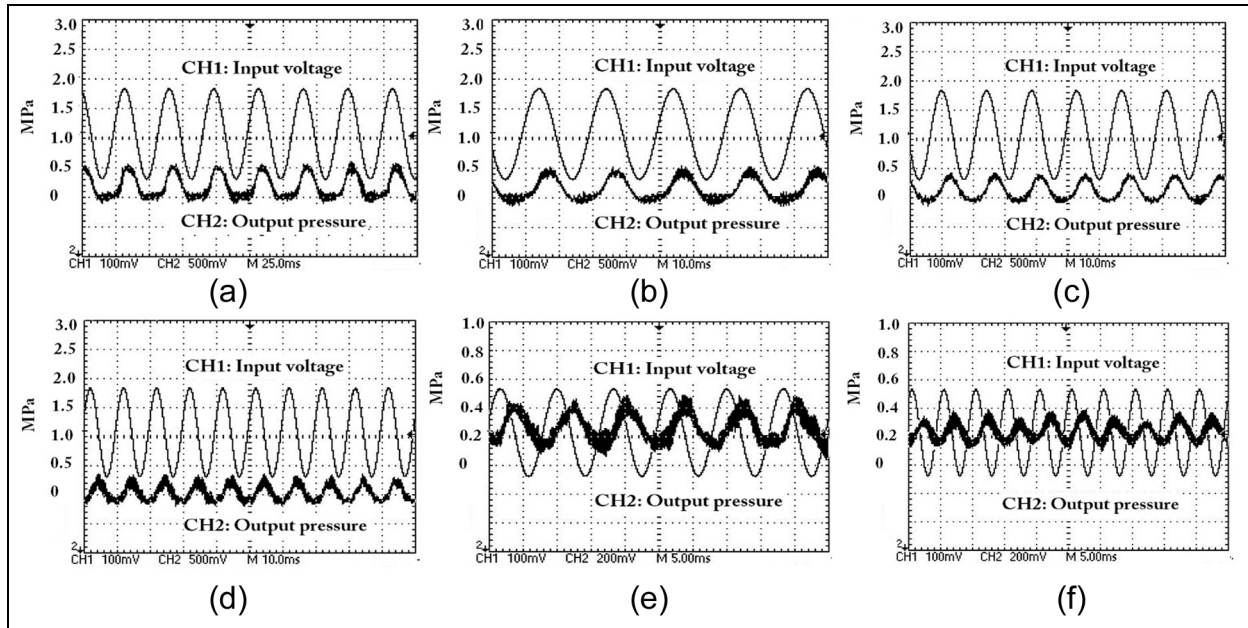


Figure 10. Output pressure response to sinusoidal input current from 0 to 1 A in an MNSP: (a) 30 Hz, (b) 50 Hz, (c) 70 Hz, (d) 100 Hz, (e) 120 Hz and (f) 200 Hz.

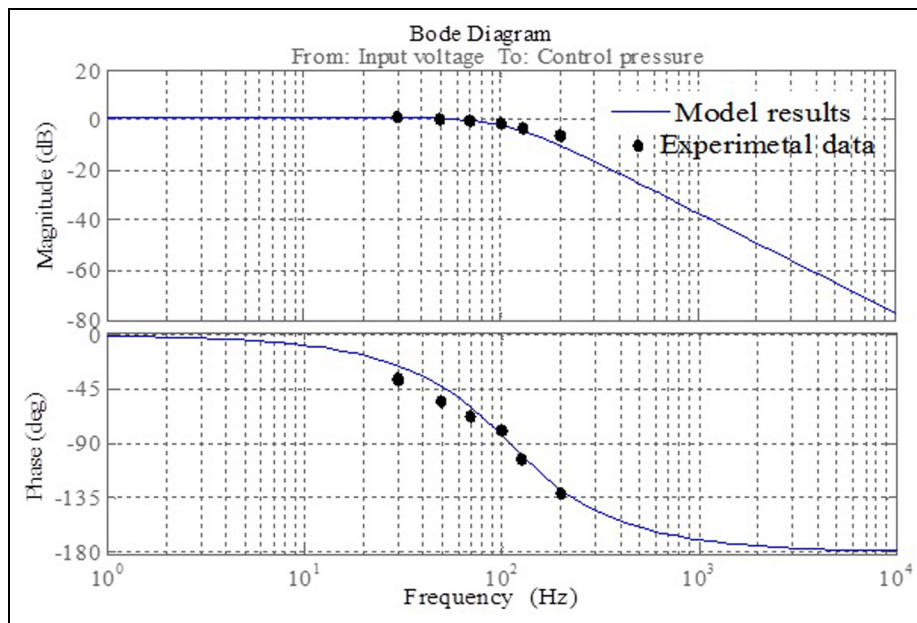


Figure 11. Amplitude–frequency curve and phase–frequency curve of an MNSP.

parameters that are sensitive to the dynamic characteristics of MNSP are found, and the accompanying rules are obtained. The diameter and the length of the GMM rod and the equivalent stiffness play more important roles regarding the step response of MNSP than the other parameters.

Based on the simulation results, by comparison with the dynamic processes of electrical–magnetic energy transformation and magnetic–hydraulic energy adjusting process, the phase angle between the magnetization of GMM rod and the output control pressure can be obtained; the phase lag angles are 36.6°, 17.2° and 5.9° with the driving frequencies 100, 50 and 10 Hz,

respectively; moreover, the phase lag angles are 53.4°, 75.4° and 84.7° with the driving frequencies 150, 200 and 250 Hz, respectively.

A dynamic performance test system of an MNSP was built, and the test data and curves using both step-input and sine-input voltages were captured by the oscilloscope, which show that the amplitude bandwidth (−3 dB) and the phase bandwidth (−90°) of an MNSP can approach 150 and 110 Hz, respectively, and agree well with the prediction results from the presented model. The research results offer a promising prospect of the novel servovalves with the high-frequency response and the large flow rate.

Declaration of conflicting interests

The author(s) declared no potential conflicts of interest with respect to the research, authorship and/or publication of this article.

Funding

The author(s) disclosed receipt of the following financial support for the research, authorship, and/or publication of this article: This work was supported by the National Natural Science Foundation of China (Grant No. 51175243).

References

- Merritt H. *Hydraulic control systems*. New York: John Wiley & Sons, 1967.
- Li S, Jiang D, Xu B, et al. 3-D magnetic field analysis of hydraulic servo valve torque motor with magnetic fluid. In: *Proceedings of the eighth international conference on electrical machines and systems (ICEMS)*, Nanjing, China, 29 September 2005, vol. 3, pp.2447–2450. New York: IEEE.
- Li BR, Gao LL and Yang G. Evaluation and compensation of steady gas flow force on the high-pressure electro-pneumatic servo valve direct-driven by voice coil motor. *Energ Convers Manage* 2013; 67: 92–102.
- Wu S, Jiao ZX, Yan L, et al. Development of a direct-drive servo valve with high frequency voice coil motor and advanced digital controller. *IEEE-ASME T Mech* 2014; 19(3): 932–942.
- Lindler JE and Anderson EH. Piezoelectric direct drive-servo valve. In: *Industrial and commercial applications of smart structures technologies*, San Diego, CA, 17 March 2002, SPIE Paper 4698-53, pp.1–9. Bellingham, WA: SPIE.
- Zhou M and Tian Y. Control of a new type of direct drive piezoelectric servo valve. In: *Proceedings of the 2004 IEEE international conference on robotics and biomimetics*, Shenyang, China, 22–26 August 2004, pp.795–798. New York: IEEE.
- Bang Y, Joo C, Lee K, et al. Development of a two-stage high speed electro-hydraulic servovalve systems using stack-type piezoelectric-elements. In: *Proceedings of the 2003 IEEE/ASME international conference on advanced intelligent mechatronics*, Kobe, Japan, 20–24 July 2003, pp.131–136. New York: IEEE.
- Sangiah D, Plummer AR, Bowen C, et al. A novel piezo-hydraulic aerospace servovalve. Part I: design and modeling. *Proc IMechE, Part I: J Systems and Control Engineering* 2013; 227(4): 371–389.
- Hiratsuka K and Urai T. Magnetic circuit design of a giant magnetostrictive actuator and application to a direct-drive servo-valve. *Nippon Kikai Gakkai Ronbunshu, B Hen/Trans Jpn Soc Mech Eng Part B* 1994; 570: 479–483.
- Urai T and Tanaka H. Development of a giant magnetostrictive tandem actuator and application to a servovalve. *Nihon Yukuatsu Gakkai Ronbunshu* 2001; 32(3): 53–57.
- Ding F, Wang C, Xu X, et al. The study of pneumatic servo valve and inchworm based on GMM. *J China Coal Soc* 2002; 27(4): 440–443.
- Wang C, Ding F and Fang P. Control pressure characteristics of nozzle flapper valve based on GMA. *J Mech Eng* 2005; 41(5): 127–130.
- Wang CL, Ding F and Cui J. Dynamic characteristics of nozzle flapper servo valve based on GMA. *J Mech Eng* 2006; 42(10): 23–26.
- Karunanidhi S and Singaperumal M. Design, analysis and simulation of magnetostrictive actuator and its application to high dynamic servo valve. *Sensor Actuat A: Phys* 2010; 157: 185–197.
- Li Y, Zhu Y and Wu H. Parameter optimization of jet-pipe servovalve driven by giant magnetostrictive actuator. *Acta Aeronaut Astronaut Sin* 2011; 32: 1336–1344.
- Zhu Y and Li Y. Development of a deflector-jet electro-hydraulic servovalve using a giant magnetostrictive material. *Smart Mater Struct* 2014; 23: 115001.
- Zhu Y, Yang X and Wang X. Development of a four-nozzle flapper servovalve driven by a giant magnetostrictive actuator. *Proc IMechE, Part I: J Systems and Control Engineering* 2015; 229(4): 293–307.
- Aung NZ and Li S. A numerical study of cavitation phenomenon in a flapper-nozzle pilot stage of an electro-hydraulic servo-valve with an innovative flapper shape. *Energ Convers Manage* 2014; 77: 31–39.
- Aung NZ, Yang Q, Chen M, et al. CFD analysis of flow forces and energy loss characteristics in a flapper-nozzle pilot valve with different null clearances. *Energ Convers Manage* 2014; 83: 284–295.
- Zhang S and Li S. Cavity shedding dynamics in a flapper-nozzle pilot stage of an electro-hydraulic servo-valve: experiments and numerical study. *Energ Convers Manage* 2015; 100: 370–379.
- Pan X, Wang G and Lu Z. Flow field simulation and a flow model of servo-valve spool valve orifice. *Energ Convers Manage* 2011; 52: 3249–3256.
- Zhu Y and Ji L. Theoretical and experimental investigations of the temperature and thermal deformation of a giant magnetostrictive actuator. *Sensor Actuat A: Phys* 2014; 218: 167–178.
- Olabi AG and Grunwald A. Design and application of magnetostrictive materials. *Mater Design* 2008; 29: 469–483.
- Pradhan SC. Vibration suppression of FGM shells using embedded magnetostrictive layers. *Int J Solids Struct* 2005; 42: 2465–2488.
- Shang X, Pan E and Qin L. Mathematical modeling and numerical computation for the vibration of a magnetostrictive actuator. *Smart Mater Struct* 2008; 17: 045026.
- Sun L and Zheng X. Numerical simulation on coupling behavior of Terfenol-D rods. *Int J Solids Struct* 2006; 43: 1613–1623.
- Valadkhan S, Morris K and Shum A. A new load-dependent hysteresis model for magnetostrictive materials. *Smart Mater Struct* 2010; 19: 125003.
- Zheng J, Cao S, Wang H, et al. Hybrid genetic algorithms for parameter identification of a hysteresis model of magnetostrictive actuators. *Neurocomputing* 2007; 70: 749–761.
- Zhou H, Zheng X and Zhou Y. Active vibration control of nonlinear giant magnetostrictive actuators. *Smart Mater Struct* 2006; 15: 792–798.
- Jiles DC. Modelling the effects of eddy current losses on frequency dependent hysteresis in electrically conducting media. *IEEE T Magn* 1994; 30: 4326–4328.
- Zhu Y and Li Y. A hysteresis nonlinear model of giant magnetostrictive transducer. *J Intel Mat Syst Str* 2015; 26(16): 2242–2255.